Eur. Phys. J. B (2019) 92: 24
https://doi.org/10.1140/epjb/e2018-90241-3

THE EUROPEAN PHYSICAL JOURNAL B

Regular Article

Ethanol chemisorption on core–shell Pt-nanoparticles: an ab initio study*

Vagner A. Rigo[1,a], Caetano R. Miranda[2], and Francesca Baletto[3]

[1] Universidade Tecnológica Federal do Paraná (UTFPR), Cornélio Procópio, Brazil
[2] Instituto de Física, Universidade de Sao Paulo (IF-USP), Sao Paulo, Brazil
[3] King's College, Physics Department, Strand WC2R 2LS, London, UK

Received 10 April 2018 / Received in final form 29 August 2018
Published online 4 February 2019

Abstract. By means of ab initio calculations, we have investigated the chemisorption properties of ethanol onto segregating binary nanoalloys (NAs). We select nanostructures with icosahedral shape of 55 atoms with a Pt outermost layer over an M-core with M = Ag, Pd, Ni. With respect to nanofilms with equivalent composition, there is an increase of the ethanol binding energy. This is not merely due to observed shortening of the Pt–O distance but depends on the nanoparticle distortion after ethanol adsorption. This geometrical distortion within the nanoparticle can be interpreted as a radial breathing, which is sensitive to the adsorption site, identified by the O-anchor point and the relative positions of the ethyl group. More interestingly, being core-dependent larger in Pd@Pt and smaller in Ni@Pt, it relates to an effective electron transfer from ethanol and the M-core towards the Pt-shell. On the view of this new analysis, Pd@Pt NAs show the most promising features for ethanol oxidation.

1 Introduction

Fuel cells can convert fuel into electricity with high efficiency, low noise, and emission rates [1–3]. Among these devices, direct ethanol fuel cells (DEFC) are particularly appealing since ethanol is a renewable fuel, can be produced from a variety of different ways, is nontoxic, and for being liquid at ambient conditions, can take advantage of the existing fuel distribution network [1,2].

Indeed, in DEFCs, ethanol chemical energy is converted to electricity using a simple operation setup [1,2], without the necessity to produce hydrogen first [1–7]. However, currently, the conversion reaction in the DEFCs stops at acetaldehyde and acetic acid, before to fully reach the ethanol oxidation to CO_2, even employing the state-of-the-art catalysts [1,3]. Considering a 1:1 mole fraction of acetaldehyde and acetic acid products, three electrons are delivered per ethanol molecule, instead of the nominal $12e^-$ [1]. On alkaline fuel cells, the ethanol oxidation reaction (EOR) kinetics at the anode is improved by adding a basic solution, e.g. KOH or NaOH, to ethanol [1]. Even so, the reaction is limited by the formation of acetic acid, delivering only $4e^-$ per ethanol. Recently, many efforts have been done on the search for promising catalytic materials to enhance ethanol kinetics [1–12].

Better performance is observed in Pt-based binary or ternary alloys against simple compounds [13,14]. Ab initio studies on Au/Pt, Pd/Pt, Au/Pd, Pd/Au, Pt/Au (111) nanofilms show that the binding energy of ethanol on dealloyed Pt-monolayer above various metallic substrates is similar to the energy on the bare Pt(111) [15]. Other strategies try to downsize Pt-based catalysts to nanoscale, where recent experimental studies showed that Pt clusters could improve the selectivity to C–C cleaving and CO_2 production along EOR [9,16,17].

The understanding of ethanol chemisorption on metallic clusters is still relatively poor and the studies are limited to a few cases, with core–shell systems often taken as promising candidates for enhancing EOR [18,19]. The magic size at which mass and specific activity peak can be optimized is still under debate. However, it is expected that Pt-nanoparticles of 2.5–2.6 nm enhance the specific activity as they balance the structural stability versus oxophilicity effects of the Pt surface [20].

Nevertheless, the atomistic details are still not fully understood yet, especially addressing the role of different chemical compositions and the variety of active sites of these nanosystems [21]. From a modelling point of view, using density functional theory (DFT) calculations with van der Waals correction, Zibordi-Besse et al. reported that the ethanol adsorption on an icosahedron of 13-atoms

* Contribution to the Topical Issue "Shaping Nanocatalysts", edited by Francesca Baletto, Roy L. Johnston, Jochen Blumberger and Alex Shluger.

[a] e-mail: vagnerrigo@utfpr.edu.br

moves from Ag, to Au, to Pd, to Cu, to Pt, then Ni, but the icosahedral symmetry is lost in both Au and Pt nanoclusters [22].

In this work, ab initio simulations have been used to evaluate ethanol adsorption on 55-atoms binary nanoalloys (NAs), with a Pt outer shell over a Ag, Pd, or Ni core. We select an icosahedral shape, to limit the study to closed-shell geometry and for being representative among Pt-structural motifs in subnano regime [23–26]. The proposed electronic and structural analysis show that all the considered NAs present a non-homogeneous radial breathing upon ethanol adsorption, but the intensity varies according to the metal-core, stronger in Pd@Pt and weaker in Ni@Pt. At the same time, a distortion within ethanol is observed with C–C and O–C more distorted in Pd@Pt and less in Ni@Pt. A linear relationship between the Pt–oxygen distance and the nanoparticle distortion is proposed to describe the system energetics. As a general result, Pd@Pt icosahedra shows adsorption properties favourable to EOR, compared the nanofilm with equivalent composition [15]. This result can be further exploited in the design of more efficient nanocatalysts, with the aim to overcome the high cost of platinum on fuel cells applications.

2 Models and methods

The spin-polarized total-energy DFT calculations [27,28] are performed using the Vienna Ab initio Simulation Package (VASP) [29,30]. We employ the generalized gradient approximation of Perdew, Burke, and Ernzerhof (PBE) [31] for the exchange-correlation functional, the projector-augmented wave method [32,33] for atomic potentials, and Gamma-point calculations for Brillouin-zone sampling. A plane-wave energy cutoff of 450 eV is used in all systems, and a vacuum slab of at least 12 Å is adopted, following convergence analysis. The van der Waals dispersion interaction is described using the Grimme formulation [34], standardized named as PBE+D3. Geometries are optimized using conjugated-gradient method until forces on atoms were lower than 0.03 eV/Å. Atomic charges are obtained through Bader analysis [35].

We consider three core–shell NAs adopting an icosahedron of 55 atoms (Ih_{55}), initially cleaved from Pt-bulk and then ionically relaxed. Ih, a Platonic solid, with twinning planes, made of 20 distorted tetrahedra sharing a common vertex, in such a way that only (111) facets are exposed. This structure is a commonly observed geometry for metallic nanoparticles and NAs, especially at small sizes [23,25,26,36]. Around the central atom, Ih shows an onion-shell motif, with a geometrical closure of the external shell after 12, 42, 92, 162,... atoms. The initial 55-atoms core@shell configurations are obtained replacing the 13-innermost atoms by Ag, Ni and Pd atoms, respectively, keeping the outermost shell atoms as Pt ones. The systems are then ionically relaxed. The formation energy of each NA composed by n Pt-shell and m M-core atoms from the gas phase can be obtained as $E_F^{\mathrm{M@N}} = E^{(\mathrm{M-core@Pt-shell})} - nE^{\mathrm{Pt-at}} - mE^{\mathrm{M-core}}$, where $E^{\mathrm{Pt-at}}$ and $E^{\mathrm{M-core}}$ is the total energy of a Pt-atom and an M-core atom in the gas phase. Accordingly, the Ag@Pt, Ni@Pt and Pd@Pt present a formation energy of −4.112, −4.904, and −4.433 eV/atom, whereas a Pt nanoparticle present −4.836 eV/atom. These information provide the energetic stability of such NAs with respect to the Pt-cluster, where the Ni@Pt is the most stable one. Various inequivalent adsorption sites are considered for ethanol adsorption following the different coordination of the Pt-anchor site [21,37–40] and the relative position of the ethyl tail. Indeed, whether for Pd@Pt, the adsorption depends mainly on where the oxygen is anchored, the orientation of the ethyl groups is fundamental in Ag@Pt and Ni@Pt. Due to its central role, we introduce a new notation/nomenclature to distinguish the non-equivalent active sites reporting explicitly where the CH_3 and CH_2 are located relative to the NA.

We name each site as [(oxygen position)]+[(CH_3 position)(CH_2 position)] and we use the labels E and V for edge and vertex Pt-atoms, respectively; and the tags *t, b, h* to identify whether the adsorption mode is atop, bridge, and hollow, respectively. For bridge and hollow, we list the relative position for all the Pt atoms involved.

The oxygen atom of ethanol onto a metallic Ih_{55} may lie on the top edge (tE), top vertex (tV), a bridge between edge and vertex (bEV), a bridge between two edge sites (bEE) and on hole site between a vertex and two edge sites (hVEE). Nonetheless, the latter and configurations where the C–C bond is radially oriented towards the NA are energetically so unfavourable that turn to be unstable over all the considered NAs. These cases are not considered further.

For the ethyl group, a hydrogen contributes significantly to the adsorption energy when it is closer than 3.2 Å from a Pt-atom. Interestingly, this is three-quarters of the bond length of an adsorbed hydrogen onto Pt(111) [41]. Table 1 reports the distances (in Å) between the Pt-atoms and the closest H-atom in CH_3 and CH_2 per each adsorption site considered. In light of the covalent bonding between the Pt-anchor and the ethanol O-atom, we consider the Pt-anchor exclusively bounded to the ethanol OH and not contributing to the weak bond of the CH-groups. Further, regarding the ethyl position on Pt-surface, three main adsorption sites are noticed. First, one surface Pt-atom can be closer to an ethanol H-atom over the evaluated sites, while other H-atoms are keeping farther. Then, two surface Pt-atoms can be at intermediate distances from a H-atom. Finally, some sites present much larger Pt–H distances for all H-atoms on CH_2 group.

Based on this, we define a bridge position whether the distances of H from the two underneath Pt-atoms are lower than 3.40 Å, and both lengths by less than 0.4 Å. The atop sites occur when one Pt–H distance in CH_3 or CH_2 is much closer compared to others (differing by more than 0.4 Å), being around the range of the sum of H and Pt van der Waals radii, 2.95 Å.

For example, the label tE+bEEbEV refers to ethanol, OH+CH_3CH_2, positioned as O on top of a Pt-edge, CH_2 making a bridge with an edge and vertex Pt, and CH_3 sees a bridge between two edge Pt-atoms instead. This

Table 1. Distances between surface Pt and the closest H-atom in CH_3 and CH_2 per each adsorption site and alloy. The label d indicates the distance between an H atom and the Pt-anchor site.

Site	CH_3	CH_2
Ag@Pt		
tE+bEEbEV	$2.81/3.11_d/3.17$	$3.01/3.17/3.26_d$
tE+tEtV	$2.75/3.12_d/3.44$	$2.66/3.31_d/3.72$
tE+tEtE	$2.45/3.12_d/3.59$	$3.18/3.25_d/3.59$
tV+tEtE	$2.84/2.99_d/3.39$	$2.65/3.42_d/4.20$
tV+tEf	$2.97_d/3.06/3.88$	$3.34_d/4.73/4.09$
tV+tEe	$2.69/3.02_d/4.02$	$3.31_d/3.83/4.32$
Ni@Pt		
tE+bEEbEV	$2.91/3.19_d/3.19$	$3.02/3.23_d/3.33$
tE+tEtV	$2.87/3.19_d/3.47$	$2.75/3.31_d/3.77$
tE+tEtE	$2.60/3.29_d/3.70$	$3.23_d/3.27/3.62$
tV+tEtE	$2.79/3.10_d/3.33$	$2.88/3.43_d/4.19$
tV+tEf	$3.06_d/3.20/3.95$	$3.47_d/4.23/4.79$
tV+tEe	$2.86/3.08_d/4.08$	$3.42_d/3.98/4.44$
Pd@Pt		
tE+bEEbEV	$2.92/3.09_d/3.16$	$2.99/3.27/3.24_d$
tE+tEtV	$2.74/3.14_d/3.48$	$2.65/3.28_d/3.68$
tE+tEtE	$2.50/3.30_d/3.45$	$3.08_d/3.24/3.69$
tV+tEtE	$2.72/3.09_d/3.43$	$2.99/3.10_d/4.09$
tV+tEf	$3.02/3.04_d/3.85$	$3.32_d/3.99/4.65$
tV+tEe	$2.66/3.04_d/3.97$	$3.27_d/3.76/4.24$

definition encloses all ethyl tail position on nanoparticles, except one (see Tab. 1), where the lowest Pt–H distance is just 1% greater than the H+Pt van der Waals radii.

Additionally, two cases present the CH_2 unbounded, with Pt–CH_2 distances greater than 3.8 Å, while CH_3 reminds onto a tE site. This happens when the C–C bond is parallel to a (111) facet, tV+tEf; or when it lies along an edge, tV+tEe. In the end, we can distinguish six stable and non-identical adsorption sites for ethanol onto an Ih_{55} NA, which are shown in Figure 1.

The adsorption energy, E_{ads}, of ethanol on a given site is given by

$$E_{ads}(\text{site}) = E_{NA+Et} - (E_{NA} + E_{Et}), \quad (1)$$

where E_{NA+Et} is the total energy after the deposition of an ethanol molecule onto the selected site, while E_{NA} and E_{Et} are the total energies of the pristine NA and the molecule in the gas phase, respectively.

In addition to the energetic analysis, we present an extensive electronic and geometrical study to address the NAs core effects, and hence to suggest the most promising chemical composition. All together energetic, electronic, and geometrical analysis allow to characterize and unravel the role of the various adsorption sites; to eventually identify a new relationship linking geometrical properties to the binding energy.

To access the electronic changes due to the ethanol adsorption, the charge redistribution is determined based on the charge difference for each atom i before and after adsorption,

$$\Delta q^i = q^i_{NA+Et} - q^i_{before}, \quad (2)$$

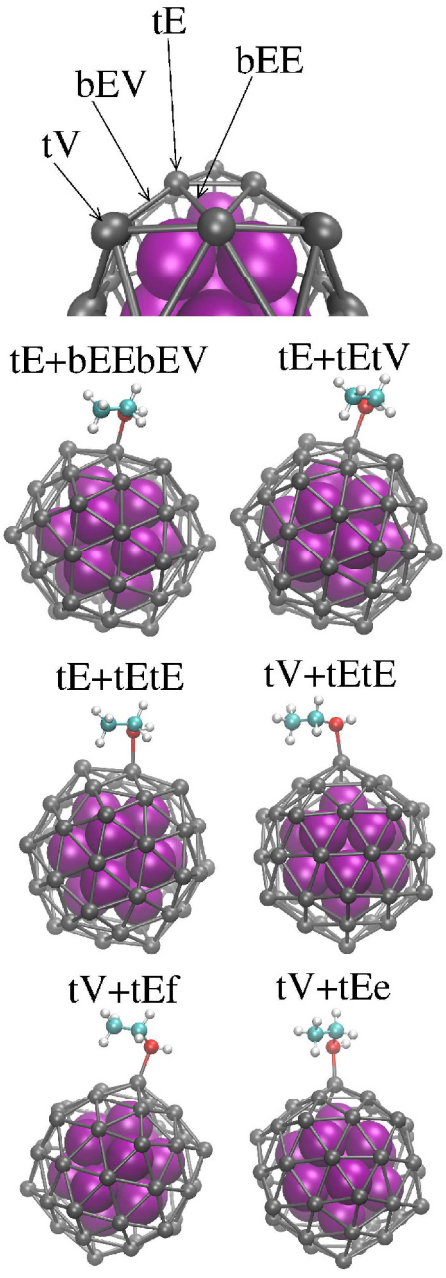

Fig. 1. The snapshot on top introduces the nomenclature adopted to identify the t (top), b (bridge) and E (edge), V (vertex) sites for ethanol adsorption onto an Ih_{55}. The six non-identical adsorption sites and their nomenclature reflecting the various orientations of the CH-groups with respect to the NA are presented below, as described in the text. The colour code presents Pt in silver, in purple the metallic core M, while red, cyan and white stand for O, C and H, respectively.

where q^i_{NA+Et} and q^i_{before} are the Bader charges of the atom i, after/before adsorption, respectively.

Additionally, we report the charge difference δq^i, between the atomic nominal valence charge, q^i_{val}, and its Bader charge after deposition. This provides a much-needed information on the charge transfer and the electrostatic effects. To address the metallic-core effects, we have

determined the charge transfer from the ethanol, δq^{Et}, from the outer Pt-layer $\delta q^{\mathrm{shell}}$, sub-surface $\delta q^{\mathrm{subshell}}$, and the core atom, δq^{core}. This was calculated by summing the δq^{i} contribution arising from atoms i belonging to a certain subsystem, for example $i \in$ Et or $i \in$ Pt − shell,

To quantitatively characterize the adsorbate/NA interaction, we have monitor how the NA geometrical features vary after adsorption. Here, we propose the radial breathing, referring to the change of the radial position $r^{i\in\mathrm{NA}}$ of the atoms i within the NA with respect to the NAs centre of mass, before and after (NA+Et) ethanol adsorption:

$$\Delta r^{i\in\mathrm{NA}} = r^{i}_{\mathrm{NA+Et}} - r^{i}_{\mathrm{before}}. \tag{3}$$

Summing over each individual atomic contribution, we obtain the net radial distortion $\mathrm{ND_{NA}} = \sum_{i\in\mathrm{NA}} \Delta r^{i}$, taken with their sign while the absolute distortion, $\mathrm{AD_{NA}}$ is $\sum_{i\in\mathrm{NA}} |\Delta r^{i}|$. Again, we can distinguish between M-core and Pt-outermost shell, $\mathrm{ND_{subshell}}$ and $\mathrm{ND_{shell}}$, simply restricting the sum over a sub-system only. Similarly, it can be applied for $\mathrm{AD_{subshell}}$ and $\mathrm{AD_{shell}}$.

Finally to estimate the geometrical distortion within the ethanol molecule, we calculate the contraction/elongation of O–C and C–C bonds of the molecule in the gas phase and after chemisorption. Let $\Delta d_{\mathrm{O-C}}$ and $\Delta d_{\mathrm{C-C}}$ be the variations in those chemical bondings, where a positive sign will stand for an elongation, while a negative sign for a contraction with respect to the gas phase.

3 Results and discussion

Figure 2 summarises the adsorption properties, both energetic and geometrical, of an ethanol molecule, the three Pt-shell M-core systems and the six adsorption sites listed in Figure 1. Let us first comment on the binding energy, reported in Figure 2a. For Pd@Pt and Ni@Pt systems, there is an enhancement up to 0.19 eV and 0.52 eV, respectively, relative to the equivalent nanofilms [15,42]. Nonetheless, it is worth to note that the adsorption on Ni@Pt surfaces did not include any van der Waals correction [42], which might play a role. At the best of our knowledge, there are no data for Ag@Pt to compare with.

On Pd@Pt, the average E_{ads} is −0.95 eV with a difference as small as 0.08 eV between tE and tV sites, and a weak if not negligible dependence on the orientation of the CH-tail. We note that this value is also higher than the binding energy calculated on an $\mathrm{Ih_{13}}$ [22]. Although out of the aim of this work, this seems to indicate a peculiar size dependence of ethanol adsorption energy. On Ag@Pt, the average distribution is of −0.70 eV and it shows a strong dependence on the CH-groups orientation, with five sites almost lying at −0.67 eV, and the tV+tEtE as low as −0.91 eV, similar to the values of Pd@Pt when oxygen is top-edge. Ni@Pt presents a similar behaviour to Ag@Pt, with an almost flat binding energy around −0.65 eV and a drop at the tV+tEtE sites of about 0.1 eV.

The Pd@Pt presents the shorter $d_{\mathrm{O-Pt}}$ values, contracted by 10% with respect to their surface equivalent. This could suggest that $\mathrm{Ih_{55}}$ is a good candidate for EOR,

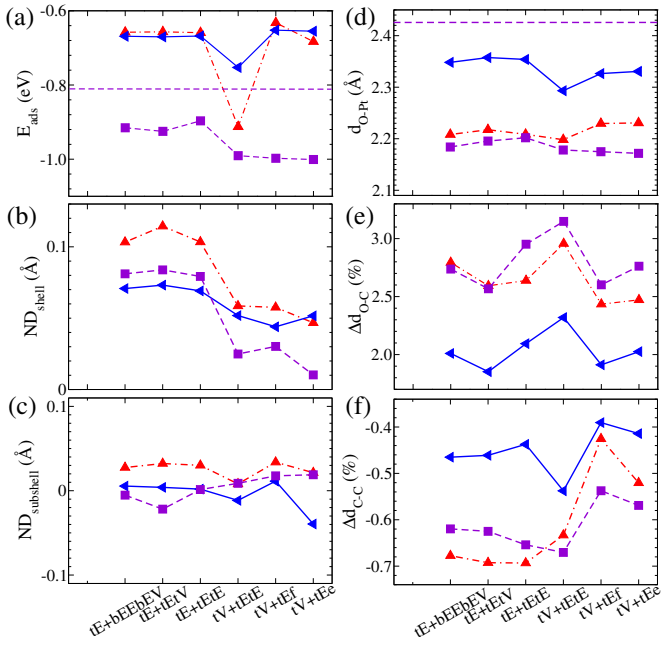

Fig. 2. (a) Adsorption energies, E_{ads}, on $\mathrm{Ih_{55}}$ Ni@Pt (blue right-triangle, full-line), Ag@Pt (red up-triangle, dashed-line), and Pd@Pt (purple square, dashed line). Purple horizontal line refers to Pd/Pt nanofilm taken from reference [15] whereas, the E_{ads} on Ni/Pt nanofilm (−0.2 eV), from [42], lies well up the scale of our graph; (b) net distortion on shell, $\mathrm{ND_{Pt}}$ and (c) core $\mathrm{ND_{core}}$; (d) bond length O–Pt-docking site, $d_{\mathrm{O-Pt}}$; (e) percentage contraction of $\Delta d_{\mathrm{O-C}}$ and (f) $\Delta d_{\mathrm{C-C}}$ after ethanol adsorption. Lines are only to guide the eye vision.

as a contraction of $d_{\mathrm{O-Pt}}$ is usually associated with an improvement of the catalytic reaction [43]. Notably, the $d_{\mathrm{O-Pt}}$ values on Figure 2d seems correlated with the E_{ads} on Figure 2a. However, the shorter $d_{\mathrm{O-Pt}}$ values occur on tV+tEtE site on Ag@Pt and Ni@Pt, and on tV+tEe site on Pd@Pt. These adsorption sites are the most stable for each nanoparticle, indicating that the $d_{\mathrm{O-Pt}}$ is relevant to the system energetics, although not exclusively.

A step forward to the understanding of the peculiar behaviour of Ag@Pt and Ni@Pt is achieved taking into account the geometrical distortion induced by ethanol onto the shell and subshell of the clusters, Figures 2b and 2c, respectively. The radial breathing, not necessarily symmetric, especially on the outer shell atoms, can represent a relevant topic for EOR. Experimentally, the radial breathing of considered subnanometre alloyed particle, which could in principle be measured by X-ray diffraction reference [44], plays a non-trivial role in the adsorption properties of ethanol and hence EOR. Notably, each NA presents a particular breathing characteristic upon ethanol adsorption. The $\mathrm{ND_{shell}}$ are site dependent and usually, the main cluster distortion happens for tE adsorption and in non-mismatched NAs. Although preserving the Ih symmetry, the $\mathrm{ND_{shell}}$ increase is higher when ethanol is adsorbed on edges rather than on vertices, and this effect is more pronounced on Ag@Pt and Pd@Pt, than Pd@Pt, probably due to their different mismatch. These results indicate a dependence between the coordination

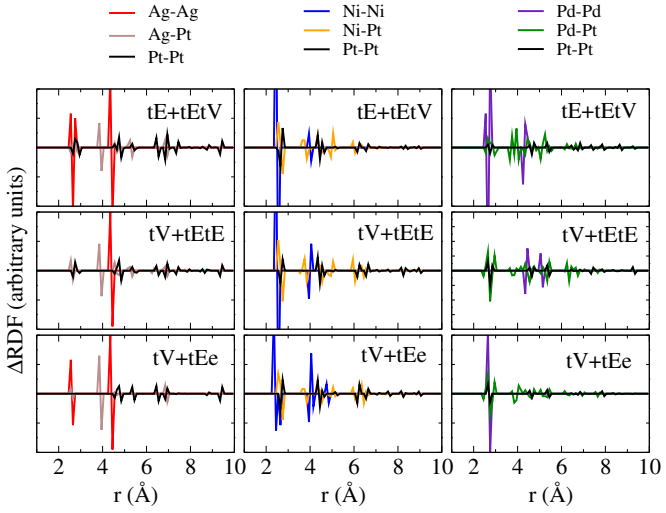

Fig. 3. Difference between the radial pair distribution functions before and after the ethanol adsorption (ΔRDF) on tE+tEtV (first), tV+tEtE (second) and tV+tEe (third line) site.

of surface atoms and the ND_{shell}. A few rearrangements occur in the subshell, as verified in Figure 2c.

To quantify the geometric modifications within the NAs upon ethanol adsorption, Figure 3 presents the radial pair distribution function difference before and after the ethanol adsorption on the cluster, $\Delta RDF(r) = RDF_{before}(r) - RDF_{after}(r)$. The result shows that ethanol adsorption on tE site results in stronger geometric modifications on clusters, in line with the ND results (Figs. 2b and 2c). Comparing NAs, the tV+tEtE site presents $\Delta RDF(r)$ modifications related to the core elements only between 2 and 4 Å on Ni@Pt. This indicates stronger core modifications on this NA, upon ethanol adsorption. Further, the modifications related with the Pt–Pt pair of atoms (shell) are weaker in the Pd@Pt, compared with Ag@Pt and Ni@Pt.

A dependence on both d_{O-Pt} and ND_{shell} in hence needed to estimate the binding energy on Pt-shell M-core NAs also with a significant lattice mismatch. This can be expressed by a linear relationship

$$E_{ads}^{Fit} = \alpha d_{O-Pt} + \beta ND_{shell} + \gamma, \quad (4)$$

where α, β and γ represent the adjusted constants, with values presented in Table 2. To evaluate the quality of equation (4) and Table 2 to reproduce the DFT data, Figure 4 presents the fitted values, E_{ads}^{Fit}, as a function of the DFT data, for each site and NA, including the linear fitting of each curve. The Ni@Pt and Pd@Pt fittings represent the E_{ads} values with notable accuracy, confirmed by the R close to one, as can see in Figure 4. Although the E_{ads}^{Fit} of Ag@Pt follows the E_{ads} trend for the most stable site, the fitting presents a poor quality, indicated by the obtained low R (0.74). Equation (4) reproduces with the energetics of the most stable site of each core composition, indicating that d_{O-Pt} and ND_{shell}, uniquely, are the key features that control the most stable position of ethanol

Table 2. Values of the adjusted constants regarding equation (4), for each evaluated NA.

Nanoalloy	α (eV/Å)	β (eV/Å)	γ (eV)
Ag@Pt	3.76	6.82	−9.57
Ni@Pt	2.32	−3.01	−5.92
Pd@Pt	2.45	0.78	−6.37

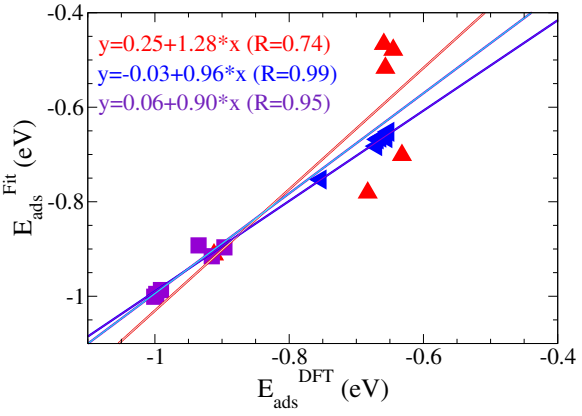

Fig. 4. Ethanol adsorption energy obtained with DFT and the adjusted equation (E_{ads}^{Fit}) for each adsorption site, with Ag@Pt as red triangle-up, Ni@Pt as blue triangle-left and Pd@Pt as purple squares. The lines correspond to linear fittings of the obtained data, for each alloy. Relevant data of fittings are presented in Table 2 and discussed along with the text.

on nanoparticles. The E_{ads}^{Fit} and DFT E_{ads} values at the most stable site results in an error of approximately 1% on Ag@Pt, and less than 1% on Ni@Pt and Pd@Pt. Further, the signal of the β coefficient in equation (4) varies according the NA (Tab. 2), evidencing the effects of the chemical composition and strain effects on the system energetics. Notably, β is positive on Pd and Ag, and negative on Ni-core. This seems to be related to the induced strain depending on the mismatch. In particular, the van der Waals radii of Ag, Ni, Pd and Pt are 2.13, 1.94, 2.05 and 2.06 Å [45]. Comparing the van der Waals radii of core elements with one Pt one, a greater mismatch is noted between Ni and Pt, indicating that equation (4) accounts partially of the strain effects on E_{ads}.

For Ag@Pt, equation (4) and Figure 3 have a smaller R than the other two alloys. This appears to be related to the dispersion interaction between the ethanol ethyl group and surface atoms, enhanced due to the strained surface of Ag-core. From Table 1, the CH_2 on a tV site reduces the distance from the Pt-surface, whereas, the CH_3 on tE is closer to Pt-surface on Ag@Pt, specially on tE+tEtV and tE+tEtE sites, and also noted on tE+tEf and tE+tEe ones.

Moving to the effects of the adsorbed molecule, from panels (e) and (f) of Figure 2, we systematically observe an elongation of the O–C, with a peak on the tV+tEtE site, and a contraction of the C–C bond. Nonetheless, Δd_{O-C} is larger in Pd@Pt, and less in Ni@Pt. We would like to comment on the different role played by the CH_x (x = 2,3) groups onto the cluster: CH_3 on tE shows a shorter

Table 3. Charge transfer upon adsorption (relative to valence charge) δq^i, and charge difference (before and after adsorption) Δq^i, for Pt-anchor, ethanol oxygen, ethanol molecule (Et), nanoparticle shell, subshell, and core-atom. Positive values indicate a gain of charge, whereas, subsystems with negative values donate charge, in the unit of electrons.

System	δq^{Pt}	δq^{O}	Δq^{Pt}	Δq^{O}	δq^{Et}	$\delta q^{\mathrm{shell}}$	$\delta q^{\mathrm{subshell}}$	δq^{core}
Ag@Pt								
tE+tEtV	−0.12	1.54	−0.17	−0.21	−0.14	3.39	−3.23	−0.02
tV+tEtE	−0.07	1.56	−0.18	−0.20	−0.12	3.41	−3.26	−0.02
tV+tEe	−0.05	1.56	−0.17	−0.19	−0.14	3.41	−3.25	−0.02
Ni@Pt								
tE+tEtV	−0.05	1.59	−0.12	−0.16	−0.10	4.22	−4.19	0.07
tV+tEtE	−0.02	1.58	−0.16	−0.17	−0.11	4.24	−4.20	0.07
tV+tEe	0.02	1.60	−0.12	−0.15	−0.11	4.24	−4.20	0.07
Pd@Pt								
tE+tEtV	−0.15	1.55	−0.18	−0.21	−0.13	2.64	−2.54	0.03
tV+tEtE	−0.07	1.54	−0.18	−0.22	−0.14	2.63	−2.55	0.06
tV+tEe	−0.07	1.54	−0.19	−0.21	−0.14	2.64	−2.43	0.06

elongation of the O–C bond. On the other hand, when both CH_2 and CH_3 are on top of a Pt-edge, $\Delta d_{\mathrm{O-C}}$ peaks. Figure 2f shows that the C–C contraction is dependent on the core composition, namely when oxygen is adsorbed on top of vertex sites, the shorter C–C bond occurs on Pd@Pt core, whereas, on edge sites, the shorter C–C bond occurs on the Ag@Pt nanoparticle. This information is important for EOR, since the elongation on the atomic distances points towards a favourable bond scission [43].

Let us now discuss the electronic contributions in the case of ethanol onto a tE+tEtV, tV+tEtE and tV+tEe sites, which is representative of a tE site, and tV ones are the best for both Ag@Pt and Ni@Pt, and Pd@Pt, respectively. Table 3 presents the charge difference of the Pt-anchor (Δq^{Pt}) site and the ethanol oxygen Δq^{O} before and after ethanol adsorption, and the charge transfer after adsorption (δq^i) of the Pt-anchor site (δq^{Pt}), ethanol oxygen (δq^{O}), and each subsystem, namely ethanol molecule (Et) and metallic inner core (subshell and core) and Pt-external layer (shell). These data provide relevant information about the systems. Interestingly, charge difference, Δq^i, shows that both the ethanol–oxygen and the Pt-anchor lose electrons after the adsorption on all NAs. Although this charge redistribution depends on the chemical core.

The charge transfer, δq^i, shows that the sub-surface layer is always positively charged, while the extra electrons migrate mainly towards the external shell. This charge transference occurs mostly because the Pauling electronegativities of Ag, Ni, Pd and Pt are 1.93, 1.91, 2,20 and 2,28, respectively. The greater electronegativity of Pt favours the Pt-shell to receive electrons from the inner atoms. As a result, a Coulomb attraction between the subshell and shell atoms takes place [46]. It is also noted that the core-atom is positively charged only at Ag@Pt, but negatively charged at Ni@Pt and Pd@Pt. The Coulomb repulsion between the core and subshell contributes to the larger net distortion (Fig. 2) of Ag@Pt. This effect is more significant in Ni@Pt, and less in Pd@Pt. As a result, the Pt-anchor is less positively charged on Ni@Pt (only 0.02 electrons), explaining the longer $d_{\mathrm{O-Pt}}$ and weaker E_{ads} obtained on Ni@Pt, compared to the other compositions seen here. This is consistent with experimental data, where the EOR on a Pt–Ni/δAl_2O_3 surface occurs only at high-temperature [47]. As recently suggested by Zhang et al., SEARS experiments can measure the charge transfer in core–shell metallic nanoparticles, such as Au@Pt [48]. At the same time, we note that the Pd-core associates significant changes of intra-ethanol bonds and a significant charge transfer from the molecule towards the nanoparticle and overall ethanol as stronger bounded to the cluster.

4 Conclusion

In summary, on the view of both the geometrical and electronic analysis, Ag@Pt and Pd@Pt Ih_{55} – where @refers to a core@shell, with a Pt-shell – present some promising features towards EOR. Ethanol shows a similar charging transfer upon adsorption on both NAs. The Pd@Pt presents the shortest $d_{\mathrm{O-Pt}}$, and the largest O–C bond when ethanol is in atop position over a five-fold vertex, whereas Ag@Pt elongates the O–C bond when the molecule is atop but on Pt-edge. Those data are explained in terms of the charging analysis, where the charge transfer of the Pt-anchor is similar to all the considered nanosystems, with 0.12 and 0.14 electrons on Ag@Pt and Pd@Pt, respectively. A model was proposed to describe the ethanol stability on each site, as a function of d_{O-Pt} and the net radial distortion in the external Pt-shell, which is able to describe with accuracy the obtained data for Ni@Pt and Pd@Pt, and Ag@Pt in a lesser account, but explaining the most stable configuration. Finally, the Ag@Pt and Pd@Pt Ih_{55} seem to be the most cost-effective material for EOR, compared to pure Pt, whereas the Ni@Pt shows much less attractive adsorption properties for this chemical reaction.

FB thanks the financial support by the UK Engineering and Physical Sciences Research Council (EPSRC), under Grants No. EP/*GO*03146/1 and No. EP/*J*010812/1. VAR and CRM thank the support of CNPq – Brazilian Federal Agency for

Scientific and Technological Development – Brazil – along this work. All the authors thanks the KCL/FAPESP agreement, and the computational support of CENAPAD-SP, UTFPR-CP, and Sdumont, in Brazil. The authors thank the financial support offered by Royal Society under the project number RG120207 and FAPESP Grant No. 17/02317-2.

References

1. L. An, T.S. Zhao, Y.S. Li, Sustain. Energy Rev. **50**, 1462 (2015)
2. S.P.S. Badwal, S. Giddey, A. Kulkarni, J. Geol, S. Basu, Appl. Energy **80**, 80 (2015)
3. J. Sun, Y. Wang, ACS Catal. **4**, 1078 (2014)
4. X.-W. Wu, N. Wu, C.-Q. Shi, Z.-Y. Zheng, H.-B. Qi, Y.-F. Wang, Appl. Sur. Sci. **338**, 239 (2016)
5. A. Verna, S. Basu, J. Power Sources **180**, 174 (2007)
6. L. An, T.S. Zhao, X.L. Zhou, L. Wei, X.H. Yan, RSC Adv. **4**, 65031 (2014)
7. L. An, Z.H. Chai, L. Zeng, P. Tan, T.S. Zhao, Int. J. Hydrogen Energy **38**, 14067 (2013)
8. L. An, T.S. Zhao, Y. Li, Q. Wu, Energy Environ. Sci. **5**, 7536 (2012)
9. R.M. Antoniassi, L. Otubo, J.M. Vaz, A. Oliveira Neto, J. Catal. **342**, 67 (2016)
10. P. Tereshchuk, J.L.F. Da Silva, J. Phys. Chem. C **116**, 24695 (2012)
11. A. Kowal, M. Li, M. Shao, K. Sasaki, M.B. Vukmirovic, J. Zhang, N.S. Marinkovic, P. Liu, A.I. Frenkel, R.R. Adzic, Nat. Mater. **8**, 325 (2009)
12. P. Tereshchuk, J.L.F. Da Silva, J. Phys. Chem. C **117**, 16942 (2013)
13. C. Engelbrekt, N. Seselj, R. Poreddy, A. Riisager, J. Ulstrupa, J. Zhang, J. Mater. Chem. A **4**, 3278 (2016)
14. L. Chen, L. Lu, H. Zhu, Y. Chen, Y. Huang, Y. Li, L. Wang, Nat. Commun. **8**, 14136 (2017)
15. A.O. Pereira, C.R. Miranda, Appl. Sur. Sci. **288**, 564 (2014)
16. C.-L. Sun, J.-S. Tang, N. Brazeau, J.-J. Wu, S. Ntais, C.-W. Yin, H.-L. Chou, E.A. Baranova, Electrochim. Acta **162**, 282 (2015)
17. Y. Guan, E.J.M. Hensen, J. Phys. Chem. C **361**, 49 (2009)
18. W. Du, G. Yang, E. Wong, N.A. Deskins, A.I. Frenkel, D. Su, X. Teng, J. Am. Chem. Soc. **136**, 10862 (2014)
19. J. Xie, Q. Zhang, L. Gu, S. Xu, P. Wang, J. Liu, Y. Ding, Y.F. Yao, C. Nan, M. Zhao, Y. You, Z. Zou, Nano Energy **21**, 247 (2016)
20. J. Perez, V.A. Paganin, E. Antolini, J. Electroanal. Chem. **654**, 108 (2011)
21. J.B.A. Davis, F. Baletto, R.L. Johnston, J. Phys. Chem. A **119**, 9703 (2015)
22. L. Zibordi-Besse, P. Tereshchuk, A.S. Chaves, J.L.F. Da Silva, J. Phys. Chem. A **120**, 4231 (2016)
23. M.G. Sandoval, R. Luna, G. Brizuela, A.O. Pereira, C.R. Miranda, P. Jasen, J. Phys. Chem. C **121**, 8613 (2017)
24. F. Baletto, R. Ferrando, Rev. Mod. Phys. **77**, 371 (2005)
25. F. Baletto, R. Ferrando, A. Fortunelli, F. Montalenti, C. Mottet, J. Chem. Phys. **116**, 3856 (2002)
26. R. Ferrando, J. Jellinek, R.L. Johnston, Chem. Rev. **108**, 845 (2008)
27. P. Hohenberg, W. Kohn, Phys. Rev. B **136**, 864 (1964)
28. W. Kohn, L.J. Sham, Phys. Rev. **140**, A1133 (1965)
29. G. Kresse, J. Hafner, Phys. Rev. B **48**, 13115 (1993)
30. G. Kresse, J. Furthmüller, Phys. Rev. B **54**, 11169 (1996)
31. J.P. Perdew, K. Burke, M. Ernzerhof, Phys. Rev. Lett. **77**, 3865 (1996)
32. P.E. Blöchl, Phys. Rev. B **50**, 17953 (1994)
33. G. Kresse, D. Joubert, Phys. Rev. B **59**, 1758 (1999)
34. S. Grimme, J. Antony, S. Ehrlich, H. Krieg, J. Chem. Phys. **132**, 154104 (2010)
35. W. Tang, E. Sanville, G. Henkelman, J. Phys. **21**, 084204 (2009)
36. C. Di Paola, R. D'Agosta, F. Baletto, Nano Lett. **16**, 2885 (2016)
37. K.E.A. Batista, M.J. Piotrowski, A.S. Chaves, J.L.F. Da Silva, J. Chem. Phys. **144**, 054310 (2016)
38. J.L.F. Da Silva, H.G. Kim, M.J. Piotrowski, M.J. Prieto, G. Tremiliosi-Filho, Phys. Rev. B **82**, 205424 (2010)
39. M.J. Piotrowski, P. Piquini, J.L.F. da Silva, J. Phys. Chem. C **116**, 18432 (2012)
40. G.G. Asara, L.O. Paz-Borbón, F. Baletto, ACS Catal. **6**, 4388 (2016)
41. G. Papoian, J.K. Nørskov, R. Hoffmann, J. Am. Chem. Soc. **122**, 4129 (2000)
42. O. Skoplyak, M.A. Barteau, J.G. Chen, Surf. Sci. **602**, 3578 (2008)
43. R. Alcalá, M. Mavrikakis, J.A. Dumesic, J. Catal. **218**, 178 (2003)
44. P.D. Jadzinky, G. Calero, C.J. Ackerson, D.A. Bushnell, R.D. Kornberg, Science **318**, 430 (2007)
45. S.S. Batsanov, Neorganicheskie Mater. **9**, 1031 (2009)
46. K.E.A. Batista, J.L.F. Da Silva, M. Piotrowski, J. Phys. Chem. C **122**, 7444 (2018)
47. E. Örücü, F. Gölaliler, A. Erhan Aksoylu, Z. Ilsen Önsan, Catal. Lett. **120**, 198 (2008)
48. Y.-J. Zhang, S.-B Li, S. Duan, B.-A. Lu, J. Yang, R. Panneerselvam, C.-Y. Li, P.-P. Fang, Z.-Y. Zhou, D.L. Phillips, J.-F. Li, Z.-Q. Tian, J. Phys. Chem. C **120**, 20684 (2016)